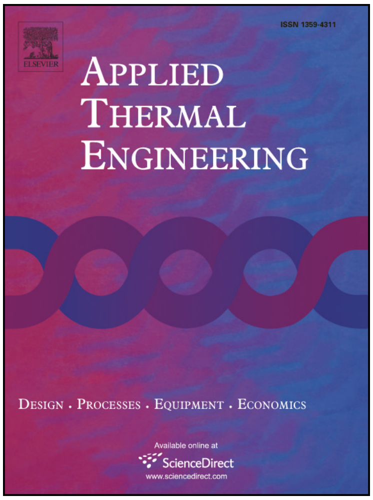

Design of redundant microvascular cooling networks for blockage tolerance

Stephen J. Pety, Marcus Hwai Yik Tan, Ahmad R. Najafi, Anthony C. Gendusa,
Philip R. Barnett, Philippe H. Geubelle, Scott R. White

PII: S1359-4311(17)32814-4
DOI: https://doi.org/10.1016/j.applthermaleng.2017.10.094
Reference: ATE 11292

To appear in: *Applied Thermal Engineering*

Received Date: 25 April 2017
Revised Date: 14 September 2017
Accepted Date: 18 October 2017

Please cite this article as: S.J. Pety, M.H. Yik Tan, A.R. Najafi, A.C. Gendusa, P.R. Barnett, P.H. Geubelle, S.R. White, Design of redundant microvascular cooling networks for blockage tolerance, *Applied Thermal Engineering* (2017), doi: https://doi.org/10.1016/j.applthermaleng.2017.10.094

Design of redundant microvascular cooling networks for blockage tolerance

Stephen J. Pety[a,d,*], Marcus Hwai Yik Tan[b,d,*], Ahmad R. Najafi[b,d], Anthony C. Gendusa[c,d], Philip R. Barnett[c,d], Philippe H. Geubelle[c,d,1], Scott R. White[c,d,1]

[a] *Department of Material Science and Engineering, University of Illinois at Urbana-Champaign, 1304 W Green St., Urbana, IL 61801, USA*
[b] *Department of Mechanical Science and Engineering, University of Illinois at Urbana-Champaign, 1206 W. Green St., Urbana, IL 61801, USA*
[c] *Department of Aerospace Engineering, University of Illinois at Urbana-Champaign, 104 S. Wright St., Urbana, IL 61801, USA*
[d] *Beckman Institute for Advanced Science and Technology, University of Illinois at Urbana-Champaign, 405 N Mathews Ave., Urbana, IL 61801, USA*

Abstract

Microvascular networks can provide host materials with many functions including self-healing and active cooling. However, vascular networks are susceptible to blockage which can dramatically reduce their functional performance. A novel optimization scheme is presented to design networks that provide sufficient cooling capacity even when partially blocked. Microvascular polydimethylsiloxane (PDMS) panels subject to a 2000 $\mathrm{W\,m^{-2}}$ applied heat flux and 28.2 $\mathrm{mL\ min^{-1}}$ coolant flow rate are simulated using dimensionally reduced thermal and hydraulic models and an interface-enriched generalized finite element method (IGFEM). Channel networks are optimized to minimize panel temperature while the channels are either clear (the O_0 scheme), subject to the single worst-case blockage (O_1), or subject to two worst-case blockages (O_2). Designs are optimized with nodal degree (a measure of redundancy) ranging from 2 – 6. The results show that blockage tolerance is greatly enhanced for panels optimized while considering blockages and for panels with higher nodal degree. For example, the 6-degree O_1 design only has a temperature rise of 7 °C when a single channel is blocked, compared to a 35 °C rise for the 2-degree O_0 design. Thermography experiments on PDMS panels validate the IGFEM solver and the blockage tolerance of optimized panels.

---

[*] These authors contributed equally to this work.
[1] Corresponding authors. Emails: swhite@illinois.edu or geubelle@illinois.edu

Preprint submitted to Applied Thermal Engineering *October 19, 2017*

Keywords: microvascular composites, optimization, redundancy, blockage tolerance

Highlights:

- For the first time, microchannel networks are optimized to tolerate blockages.
- Optimized cooling panels show reduced temperature rise when a channel is blocked.
- Blockage tolerance increases further for networks with higher nodal degree.
- Temperature rise values range from 7 °C (optimized) to 35 °(reference).
- A new high-speed fabrication technique is used to validate the optimized designs.

---

1. Introduction

Microvascular networks can be used to provide efficient cooling for batteries [1, 2, 3, 4], fuel cells [5, 6, 7], and structural composites operating under high heat fluxes [8, 9, 10, 11]. Vasculature also enables a variety of other functions such as self-healing [12], damage sensing [13], and electromagnetic modulation [14, 15]. However, the small size of microchannels makes them susceptible to blockages from contaminants or damage [16, 17, 18, 19]. Blockages in cooling networks can lead to a sudden increase in panel temperature, especially for channels with few interconnections [20]. Blockages are also a major concern in self-healing systems to ensure robust and repeated healing capability [12, 21].

In nature, blockages in vascular networks are circumvented through network redundancy. For example, palmate leaves possess dense venation to allow for water and nutrient transport even if the main vein is damaged [22]. Mammal cardiovascular systems similarly have dense, hierarchical vasculature to allow for blood flow even when arteries or veins become clogged [23, 24, 25]. Inspired by nature, Katifori et al. [26] and Corson et al. [27] optimized branching channel networks to minimize pumping pressure while channels were randomly blocked. Both studies generated leaf-like networks containing dense branching and loops, substantiating the idea that natural vascular networks evolved to resist blockages.

A limited number of studies have been performed to design similar redundant networks for cooling applications [20, 28, 29]. For example, Aragon et al. [28] optimized 2D microvascular networks for objective functions of flow uniformity, pumping pressure, and channel volume fraction. Networks with higher redundancy were found best for addressing all three objectives at once. However, only one study has simulated how blockages affect cooling performance [20], and no study has optimized a cooling network for blockage tolerance. In addition, no experimental studies have been performed on the blockage tolerance of microvascular cooling panels.

Here, a novel optimization scheme is presented to minimize the temperature of a cooling panel while subject to different numbers of blockages. The thermal field in the panel is obtained from an interface-enriched generalized finite element method (IGFEM) solution of dimensionally reduced thermal and hydraulic models [30, 31]. The IGFEM solver allows for the use of a nonconforming mesh while the dimensionally reduced models collapse the channels into line sources/sinks. To perform gradient-based optimization, we first perform a sensitivity analysis on the discretized weak form resulting from the IGFEM. The sensitivity analysis lets us obtain the gradient of the objective function with respect to the design parameters that define the geometry of the embedded network. The objective function is the p-norm of temperature, a differentiable alternative of the maximum temperature. The sequential quadratic programming algorithm is used as the gradient-based optimization algorithm.

Channel networks are optimized using three schemes. First, a traditional optimization scheme (O_0) is performed to reduce the maximum temperature while the channels are clear. This technique has already seen success for optimizing channel networks in battery cooling panels [1]. Panels are then optimized while the channel network is subject to either a single blockage (the O_1 scheme) or two simultaneous blockages (the O_2 scheme).

Simulations are performed with a panel size (75 mm x 75 mm in-plane), applied heat flux (2000 $\mathrm{W\,m^{-2}}$), and coolant flow rate (28.2 mL $\mathrm{min^{-1}}$, or 0.5 g $\mathrm{s^{-1}}$) representative of fuel cell cooling panels [5]. Microvascular polydimethylsiloxane (PDMS) was used due to the ease of manufacturing and ability to create the blockages needed for validation. The panels contain 2D channel networks with interior nodal degree (a measure of redundancy) ranging from 2 – 6.

This manuscript is organized as follows. The simulation framework is first described (§2.1) while the dimensionally reduced models and IGFEM technique are detailed in the Appendix. The optimization scheme is summarized (§2.2) followed by a description of the problem setup and reference designs (§2.3). The fabrication of PDMS cooling panels using a novel technique involving laser cutting and secondary bonding, and their testing for thermal performance are presented next (§2.4). Validation of simulations, optimization results, and blockage tolerance studies are presented in the results (§3).

2. Materials and methods

2.1. Simulation setup for microvascular PDMS panels

The modeled geometry is shown in Fig. 1 and the adopted dimensions, boundary conditions, and material properties used are listed in Table 1. A 75 mm x 75 mm x 3.8 mm PDMS microvascular panel was heated from below with a 2000 W m^{-2} heat flux over the central 50 mm x 50 mm region. Water/glycol coolant was pumped through a 2D microvascular network formed by 0.81 mm x 0.55 mm interconnected rectangular channels. Water/glycol is a common coolant for cooling batteries [4] and fuel cells [6].

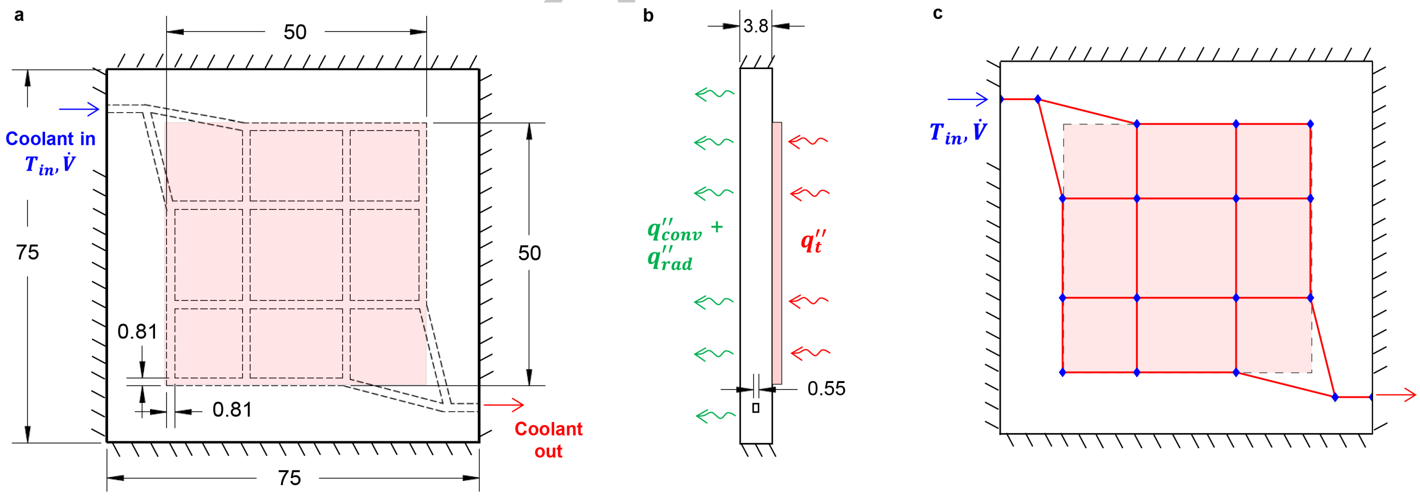

Figure 1: Schematics of microvascular PDMS cooling panels. a) Top and b) side view of the cooling panel with dimensions in mm. The panel is heated in the central 50 mm x 50 mm region from below while coolant circulates at a set inlet temperature and flow rate. The top of the panel is open to convection/radiation and the sides are insulated. c) Schematic of the simulated panel, with the channels modeled as line sources/sinks.

Table 1: Parameters for cooling simulations.

Parameter	Value
Sample dimensions in mm	
Panel width and length	75
Panel thickness t	3.8
Nominal channel width b_{nom}	0.81
Nominal channel height a_{nom}	0.55
Reduced channel width b_{red}	0.68
Reduced channel height a_{red}	0.53
Boundary conditions	
Baseline heater power q_t'' ($\mathrm{W\,m^{-2}}$)	2000
Heater width and length (mm)	50
Convection coefficient $\tilde{h}$ ($\mathrm{W\,m^{-2}\,K^{-1}}$)	15
Emissivity for top face ϵ	0.97
Ambient temperature T_∞ (°C)	22
Sides of panel	Insulated
Baseline coolant flow rate $\dot{V}$ ($\mathrm{mL\,min^{-1}}$)	28.2
Coolant inlet temperature T_{in} (°C)	22
Outlet pressure (Pa)	0
Coolant - 50:50 water:ethylene glycol [4]	
Density ρ ($\mathrm{kg\,m^{-3}}$)	1065
Viscosity μ ($\mathrm{kg\,m^{-1}\,s^{-1}}$)	$0.0069(T/273)^{-8.3}$
Specific heat capacity c_p ($\mathrm{J\,kg^{-1}\,K^{-1}}$)	3494
Panel - Polydimethylsiloxane [32]	
Thermal conductivity κ ($\mathrm{W\,m^{-1}\,K^{-1}}$)	0.27

The top panel surface was open to the environment where heat losses occur through both natural convection to the surrounding air (q''_{conv}) and radiation from the panel surface to its cooler surroundings (q''_{rad}). The convective heat transfer coefficient $\tilde{h} = 15$ W m^{-2} K^{-1} was found by fitting to experimental data and the panel emissivity ϵ was set to 0.97 to represent the matte black paint used on experimental specimens. The sides of the sample were insulated and an inlet temperature of 22 °C was specified based on the average inlet temperature measured during experiments.

The coolant flow rate ranged from 0 mL min^{-1} to 56.4 mL min^{-1} for the validation study and was set to 28.2 mL min^{-1} for the optimization study. The flow rate was chosen to be held constant during optimization instead of pumping power, since the pumping power for these microvascular networks is very small (on the order of 10 mW). Pumps for these networks would thus be more limited by flow rate than by power.

To increase simulation speed, the temperature distribution of the panel was solved using dimensionally reduced thermal and hydraulic models (presented in Appendix A.1) solved with the aid of an interface-enriched generalized finite element method (IGFEM) (summarized in Appendix

A.2). This technique collapses the channels into line sources/sinks and discretizes the domain with a mesh that does not conform with the network (see Fig. 1c). The hydraulic model assumes laminar flow, since the maximum Re number for any studied case is 500. Simulations were performed using structured triangular meshes with 40 divisions in both planar directions.

Due to the nonlinear nature of radiative heat loss, two models were used to simulate radiation. To improve efficiency, a linearized model was used for optimizations. A nonlinear thermal model was then used to obtain more accurate thermal fields for the final optimized designs (see description of these models in Appendix A.2). All presented thermal profiles and temperature data are from the nonlinear model unless otherwise noted.

After the solution of the thermal field, the pumping pressure was calculated assuming uniform fluid viscosity throughout the channels (see Appendix A.1.2). The hydraulic model assumes that flow rate linearly scales with pressure drop according to fully developed Poiseulle flow [33]. Viscosity was evaluated at the average fluid temperature using the temperature-dependent viscosity in Table 1 [4]. Two sets of channel dimensions were simulated to provide bounds for pressure: one with nominal (average) channel dimensions of 0.81 mm x 0.55 mm and one with channel dimensions reduced by one standard deviation (0.68 mm x 0.53 mm). The variance in channel dimensions results from the laser cutting technique described in §2.4. The reduced dimensions were simulated since the pumping pressure scales with the inverse fourth power of the channel diameter, so any slight restriction in experimental channel dimension can dramatically increase the pressure. Pety et al. also demonstrated that reduced dimensions provide good bounds for pumping pressure in microvascular carbon fiber panels [3].

2.2. Gradient-based optimization technique

The IGFEM solver, sensitivity analysis, and gradient-based sequential quadratic programming algorithm available in MATLAB [34] were combined to solve two optimization problems. The design parameters were the locations of channel nodes, and the desired objective function was to minimize the maximum panel temperature T_{max}. However, since T_{max} is not differentiable, it was replaced with the differentiable p-norm

$$\|T^{(h)}\|_p = \left(\int_\Omega T^{(h)^p} \mathrm{d}\Omega\right)^{1/p}, \tag{1}$$

where $T^{(h)}$ is the IGFEM-predicted panel temperature and p is an integer sufficiently large to represent the behavior of the maximum temperature. Ω denotes the panel domain. Based on previous work [1], we choose $p = 8$.

First, optimizations were performed with unblocked channels, denoted as the O_0 scheme. Denoting the design parameters by $\boldsymbol{d} = \{d_1, ..., d_{n_d}\}$ and the nodal coordinates of the mesh by $\boldsymbol{X}$, the optimization problem is expressed as

$$\begin{aligned} \min_{\boldsymbol{d}} \quad & \|T^{(h)}\|_p(\boldsymbol{X}(\boldsymbol{d}), \boldsymbol{d}), \\ \text{such that} \quad & \boldsymbol{g}(T^{(h)}(\boldsymbol{X}(\boldsymbol{d}), \boldsymbol{d}), \boldsymbol{X}(\boldsymbol{d}), \boldsymbol{d}) \leq 0, \end{aligned} \tag{2}$$

where $\boldsymbol{g} \leq 0$ is a vector of constraints.

Optimizations were also performed with one or more channels fully blocked. Let $\boldsymbol{b}$ be a bit vector with n_{ch} entries where 1 on the jth position means that the jth channel is blocked and 0 otherwise. Let $\mathcal{B}$ be a finite set of bit vectors $\{\boldsymbol{b}^{(1)}, \boldsymbol{b}^{(2)}, ..., \boldsymbol{b}^{(n_\mathcal{B})}\}$ representing $n_\mathcal{B}$ blockage scenarios. The problem of designing for blockage tolerance can be thought of as the minimization of the worst "damage" resulting from predetermined blockage scenarios. One quantification of the "damage" is the maximum temperature in the domain, captured by $\|T^{(h)}\|_p$. The optimization problem is then formulated as

$$\begin{aligned} \min_{\boldsymbol{d}} \max_{\boldsymbol{b} \in \mathcal{B}} \quad & \|T^{(h)}\|_p(\boldsymbol{b}, \boldsymbol{X}(\boldsymbol{d}), \boldsymbol{d}), \\ \text{such that} \quad & \boldsymbol{g}(T^{(h)}(\boldsymbol{X}(\boldsymbol{d}), \boldsymbol{d}), \boldsymbol{X}(\boldsymbol{d}), \boldsymbol{d}) \leq 0, \end{aligned} \tag{3}$$

where the first argument after the p-norm emphasizes that the predicted temperature is a function of the bit vector $\boldsymbol{b}$. The seemingly formidable optimization problem (3) was converted into the following simpler optimization problem [35, 36], referred to as the O_i scheme, where $i > 0$ is the maximum number of blockages in $\mathcal{B}$:

$$\begin{aligned} \min_{\boldsymbol{d},z} \quad & z \\ \text{such that} \quad & \|T^{(h)}\|_p(\boldsymbol{b},\boldsymbol{X}(\boldsymbol{d}),\boldsymbol{d}) - z \leq 0, \quad \forall \boldsymbol{b} \in \mathcal{B} \\ \text{and} \quad & \boldsymbol{g}(T^{(h)}(\boldsymbol{X}(\boldsymbol{d}),\boldsymbol{d}),\boldsymbol{X}(\boldsymbol{d}),\boldsymbol{d}) \leq 0. \end{aligned} \tag{4}$$

For the remainder of the paper, the different blockage scenarios are described using the notation summarized in Table 2. The design obtained from the O_i optimization and operated in the blockage scenario $\boldsymbol{b}$ is denoted by $O_i(\boldsymbol{b})$. Let $\boldsymbol{c}$ be a bit vector with all entries equal to 0. Thus $O_i(\boldsymbol{c})$ represents a design operating with clear channels. For a given design, define $\boldsymbol{w}$ as a bit vector containing a single unity entry that maximizes T_{max} over $\mathcal{S}$, i.e., $\boldsymbol{w} = \arg\max_{\boldsymbol{B}\in\mathcal{S}} T_{\max}(\boldsymbol{b})$. Thus $O_i(\boldsymbol{w})$ is a design operating in the worst case single blockage scenario of $\mathcal{S}$. Finally, $\boldsymbol{w_2}$ is a bit vector containing two unity entries that maximizes T_{max} over $\mathcal{S}$, meaning $O_i(\boldsymbol{w_2})$ is a design operating with the worst case double blockage scenario.

The sensitivity analysis required by the optimization algorithm was developed using the linear radiation model for increased efficiency. The sensitivity analysis is presented in detail in [1].

Table 2: Summary of design notations.

Notation	Description
R	Reference design
O_0	Design optimized for clear channels
O_1	Design optimized for a single worst-case blockage
O_2	Design optimized for two worst-case blockages
$O_i(\boldsymbol{c})$	O_i design operating with clear channels
$O_i(\boldsymbol{w})$	O_i design operating with a single worst-case blockage
$O_i(\boldsymbol{w_2})$	O_i design operating with two worst-case blockages
Dn	Degree-n design

2.3. Optimization problem setup and reference designs

Optimizations were performed on reference channel networks with interior nodal degrees (a measure of redundancy) ranging from 2 to 6 as shown in Fig. 2a-e. Nodal degree is defined as the number of channels incident upon any of the four interior nodes. Degree-n designs will henceforth be noted by Dn.

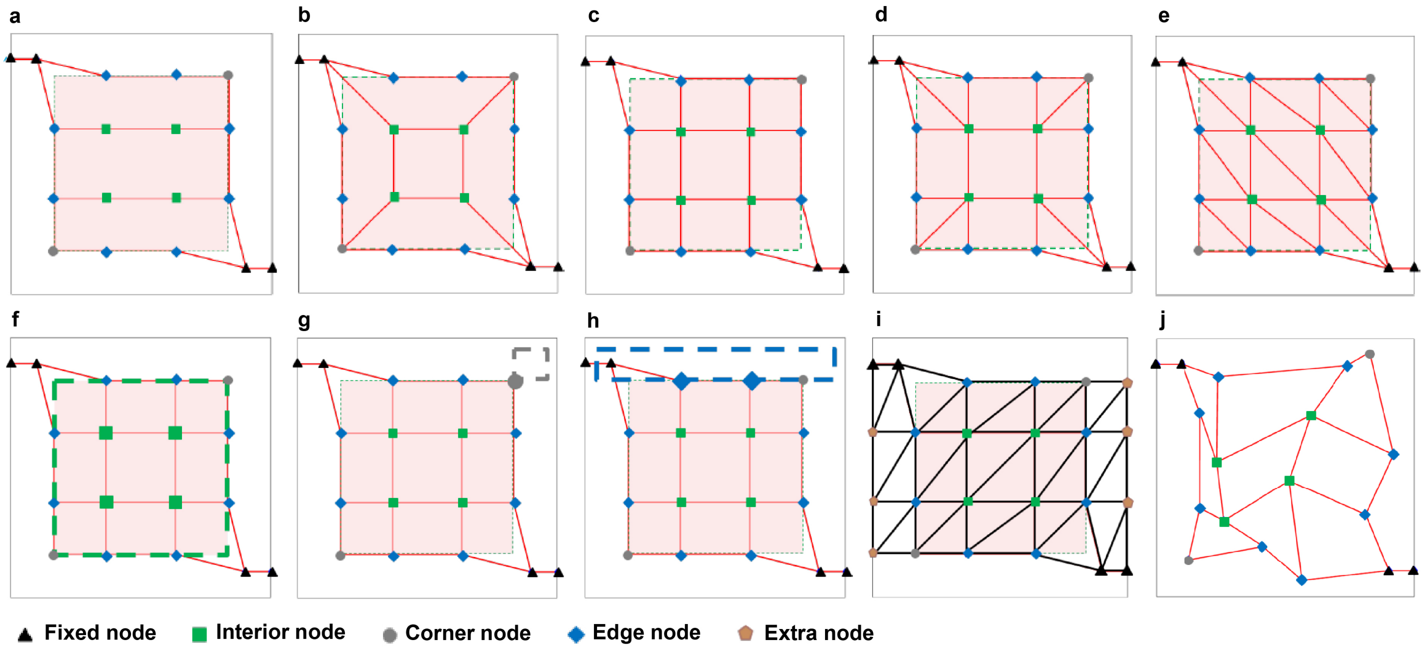

Figure 2: Reference network configurations and constraints on nodal position. Reference networks are shown for nodal degrees of a) two ($D2$), b) three ($D3$), c) four ($D4$), d) five ($D5$), and e) six ($D6$). Bounding boxes are shown for f) interior nodes, g) the top right corner node, and h) the top two edge nodes for the $D4$ network design. i) Extra nodes and triangles used to prevent self-intersection of channels. j) Example of a randomly generated initial $D4$ channel design.

The nodes defining the embedded network were constrained during optimization as follows. The inlet and outlet nodes were fixed, and interior nodes were allowed to move within the central region delineating the heater as shown in Fig. 2f. Corner and edge nodes were restricted to move outside of the heated zone as shown in Fig. 2g-h. For example, the top right corner node was confined in the bounding box $\{62.5 \leq x \leq 72.5\,\text{mm}, 62.5 \leq y \leq 72.5\,\text{mm}\}$ (Fig. 2g) and the two upper edges nodes were confined to $\{2.5 \leq x \leq 72.5\,\text{mm}, 62.5 \leq y \leq 72.5\,\text{mm}\}$ (Fig. 2h).

To avoid the "self-crossing" of channels, geometrical constraints were applied to triangles constructed from the channels as shown in Fig. 2i. The constraints were (i) the interior angles of the triangles must be $> 10°$ and (ii) the area of each triangle must be $> 0.001\times$ the area of the domain. At least 48 distinct initial designs were generated for each optimization by shuffling the control points within non-overlapping boxes. An example of an initial design is shown in Fig. 2j.

For optimizations with blockages, we considered the collection of blockages $\mathcal{B}$ to consist of single-channel blockages (the O_1 scheme) or double-channel blockages (the O_2 scheme) that exclude the inlet and outlet channels. The number of possible single-channel blockages ranges from 16 for the $D2$ design to 31 for the $D6$ design. Double-channel blockages were only considered for the $D6$ design, where the total number of blockage scenarios is 465.

2.4. Fabrication and testing of microvascular PDMS panels

2.4.1. Fabrication of microvascular panels

Microvascular PDMS panels were prepared using a novel technique combining laser cutting with secondary bonding (Fig. 3). Commercial PDMS sheets (McMaster-Carr, part # M8414) of 0.5 mm and 1.6 mm thickness (nominal) were cut into 82 mm x 82 mm squares. A 0.5 mm thick sheet was stacked onto a 1.6 mm thick sheet (Fig. 3a) and a 90 W CO_2 laser cutter (Full Spectrum Laser, Pro Series, 48" x 36") was used to cut a path of the desired network into the top piece of PDMS. One pass of the laser was performed at 30% power and 100% speed. The PDMS inside the cut path was manually removed with tweezers (Fig. 3b). For some samples, a full blockage was introduced into one channel by leaving a 5 mm long uncut piece of PDMS inside. Networks were designed in SolidWorks 2014 and the laser cutter was controlled using RetinaEngrave (2011) software. The average network width was 0.81 mm with a standard deviation of 0.13 mm based on 70 measurements across 5 samples.

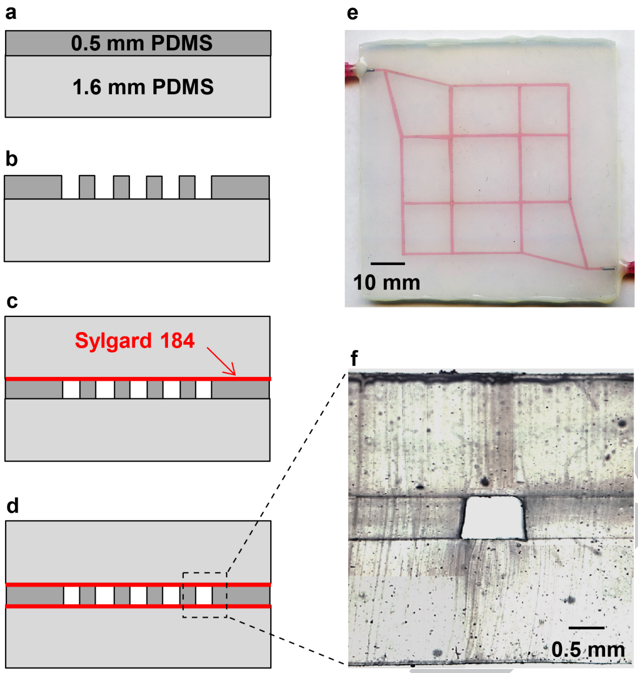

Figure 3: Fabrication of microvascular PDMS panels. a) A thin (0.5 mm) PDMS sheet is stacked on top of a thick (1.6 mm) PDMS sheet. b) The top sheet is laser-cut to form a vascular network. c) A thick (1.6 mm) PDMS sheet is bonded to the top using spin-coated Sylgard 184 adhesive. d) The original backing is removed and another thick (1.6 mm) PDMS sheet is bonded in its place. e) Image of microvascular PDMS panel filled with ethanol mixed with Red 3 and Red 40 dyes for visualization. f) Cross-sectional micrograph showing one 0.81 mm x 0.55 mm channel.

Next, Sylgard 184 PDMS adhesive (Dow Corning) was mixed 10:1 base:hardener by hand, degassed for 20 min, and spin-coated (SCS Spin Coater model 6800) onto a 1.6 mm thick sheet of commercial PDMS. Spin coating was performed at 4000 rpm for 200 s to produce a ca. 5 µm thick adhesive layer. The adhesive-coated PDMS layer was then placed on top of the cut PDMS layer, a weight was added to provide 20 kPa pressure, and the adhesive was cured for 4 h at 80 °C (Fig. 3c). After cure, the original 1.6 mm thick PDMS substrate was removed and a separate 1.6 mm thick PDMS piece was bonded in its place using the same spin-coating procedure (Fig. 3d). Panels were then cut to a final size of 75 mm x 75 mm (see sample image in Fig. 3e). Final panels were 3.79 ± 0.07 mm thick and contained rectangular microchannels that were 0.81 ± 0.13 mm wide and 0.55 ± 0.03 mm tall (see micrograph in Fig. 3f).

This fabrication technique is rapid and inexpensive, since the only materials needed are commercial silicone sheets and a small amount of adhesive. The use of a CAD-controlled laser cutter also decouples network complexity from cost.

2.4.2. Thermal testing of microvascular panels

Needle fittings (20 gauge) were inserted into the inlet and outlet of each panel and sealed by applying epoxy adhesive (Loctite E-120hp) around the perimeter of the panel. One surface of the panel was painted matte black (Krylon) for thermal imaging. Fig. 4a shows the experimental setup used for cooling tests. The panel was coupled to a 50 mm x 50 mm polyimide flexible heater (Omega, part # KH-202/10) using thermal grease (Omega, part # Omegatherm 201) and placed on a balsa wood platform. An acrylic plate with a 74 mm x 74 mm viewing window was secured on top of the specimen to prevent the sample edges from warping during testing (Fig. 4b). The heat flux generated by the heater was controlled by adjusting voltage with a Variac variable transformer (Staco Energy Products Co., Type L1010). Voltage values were correlated to heat flux values using the equation $q'' = V^2/RA$ where q'', V, R, and A respectively denote areal heat flux, voltage, heater resistance, and heater area.

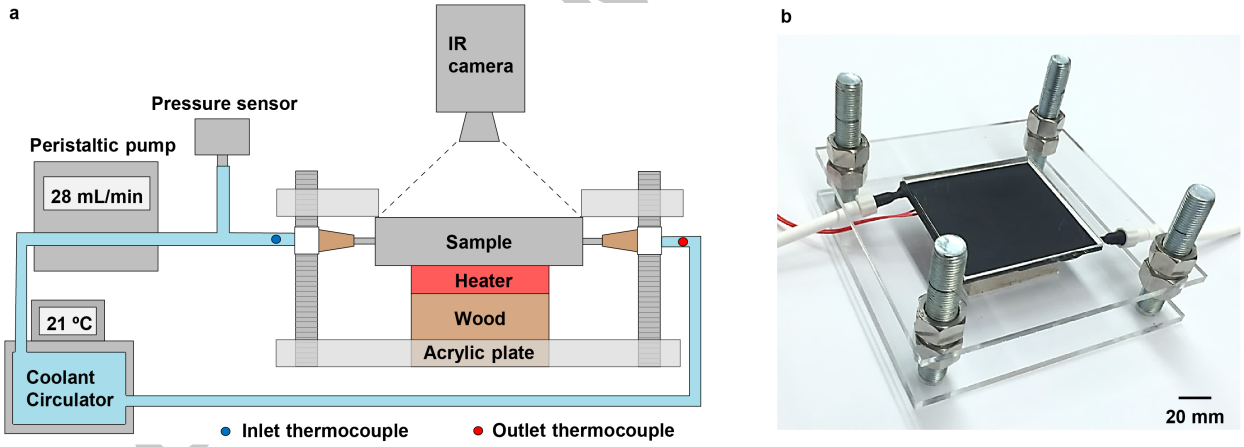

Figure 4: Experimental cooling setup. a) Schematic of experimental setup in which panel surface temperature is monitored with an IR camera, coolant temperature is monitored with inlet and outlet thermocouples, and pumping pressure is monitored with a pressure transducer. An acrylic fixture is used to prevent panel out-of-plane warpage. b) Isometric view of panel in the acrylic fixture.

A mixture of 50:50 water:ethylene glycol (Macron Chemicals) was stored in a circulator (Julabo, Model F32-HP) refrigerated to 21 °C and pumped through the panel with a peristaltic pump (Cole-Parmer Masterflex, Model EW-07551099). Coolant inlet and outlet temperature were measured with ungrounded T-type thermocouples (Omega part # TMQSS-020U-36, accuracy of ± 0.5 °C) inserted into the tubing lines. Thermocouple readings were processed with four-port thermocouple readers (Phidgets Inc., model # 1048) and LabVIEW 2013.

Pumping pressure was measured using a wet/wet gage pressure transducer (Omega part # Px26, ± 1 kPa) with a range of 0 – 103 kPa. Transducer readings were processed using a DAQ board (National Instruments, NI USB-6251) and LabVIEW 2013. To account for the pressure drop through the needle fittings, calibration tests were performed in which coolant was pumped through two connected fittings. Final pressure drop values through a given network were found by taking the raw pressure reading and subtracting the pressure needed to pump coolant through the fittings alone. Fig. S1 plots the pressure adjustment required for different flow rates.

The surface temperature of the panel was recorded with an infrared (IR) camera (FLIR Model SC620, absolute temperature accuracy of ± 2 °C). Experiments were performed to measure panel temperature, coolant temperature rise ΔT_c, and pumping pressure at steady-state. The cooling efficiency η of the panel was then calculated as the ratio of the heat flux absorbed by the channels q_c to the total applied heat flux q_t, i.e.,

$$\eta = \frac{q_c}{q_t} = \frac{\dot{m} c_p \Delta T_c}{q_t}, \tag{5}$$

where $\dot{m}$ and c_p respectively denote the mass flow rate and specific heat capacity of the coolant.

3. Results and discussion

3.1. Validation of the reference panel at different flow rates

Experiments and simulations were first performed on the reference $D4$ design to validate the IGFEM solver. Simulated and experimental thermal profiles at the baseline flow rate of 28.2 mL min^{-1} (0.5 g s^{-1}) agree well, as shown in Fig. 5. Thermal agreement was maintained from 0 to 56.4 mL min^{-1} flow rate as presented by a plot of T_{max} in Fig. 6a. Simulated data is presented for both the linear radiation model, which is used in optimizations to increase simulation speed, and the nonlinear radiation model, which is used to calculate thermal profiles for the final optimized designs. The maximum temperature equilibrates to ca. 110 °C at zero flow rate, decreases quickly with increasing flow rate, and then plateaus to ca. 60 °C at flow rates above 20 mL min^{-1}. Good agreement is achieved between experiment and simulations using both radiation models.

Experimental and numerical values of the pumping pressure (i.e. the pressure drop through the channel network) are shown in Fig. 6b. The IGFEM results correspond to both the nominal (average) channel dimensions and the channel dimensions reduced by one standard deviation. The pressure rises linearly with the flow rate as expected. The simulations bound the experimental data, with the reduced channel dimensions providing the closet fit.

Fig. S2 shows further agreement between simulation and experiment for coolant temperature rise ΔT_c and cooling efficiency η vs. flow rate. The coolant temperature rise decreases rapidly at first and then plateaus, similar to T_{max}. The cooling efficiency increases to ca. 80% and then plateaus above 20 mL min^{-1} flow rate.

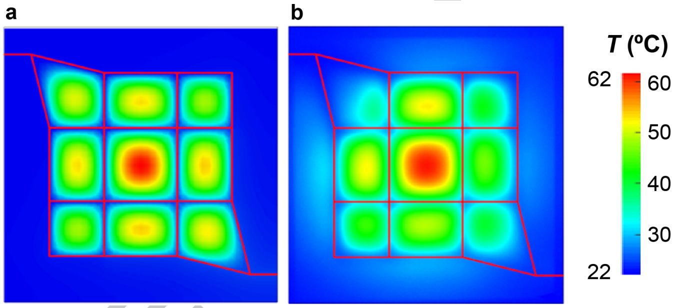

Figure 5: Comparison of thermal profiles for the $D4$ R design from a) simulation and b) experiment at an applied heat flux of 2000 $\text{W}\,\text{m}^{-2}$ and a flow rate of 28.2 $\text{mL}\,\text{min}^{-1}$.

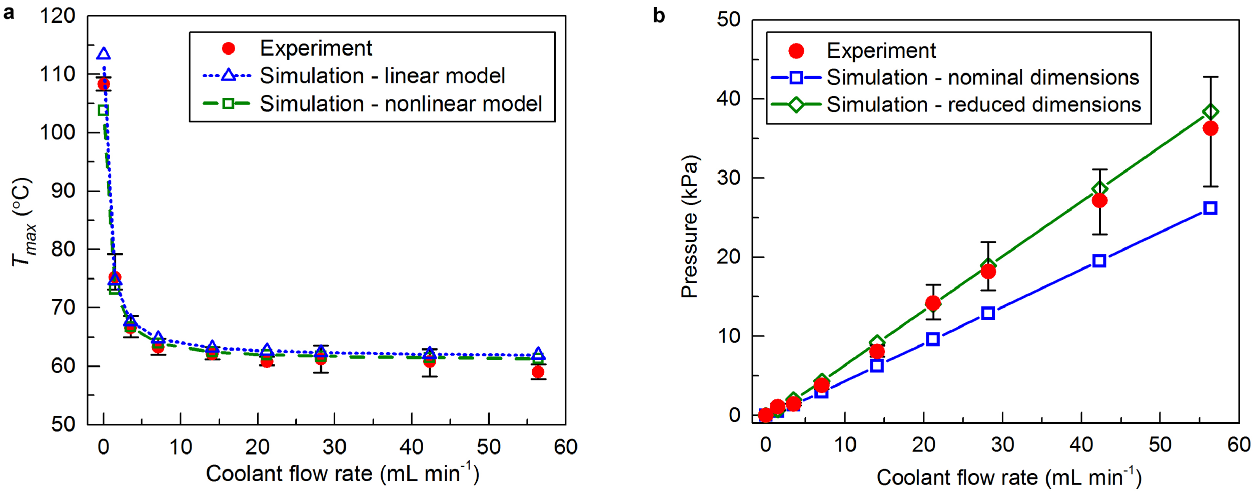

Figure 6: Validation of studies for the $D4\ R$ panel at different flow rates. a) Experimental T_{max} values compared to simulated values using both the linear and nonlinear radiation models. b) Experimental pumping pressure compared to simulated values using both nominal channel dimensions (0.81 mm x 0.55 mm) and channel dimensions reduced by one standard deviation (0.68 mm x 0.53 mm). Experimental error bars represent the maximum and minimum values for three replicate panels. The applied heat flux is 2000 $\mathrm{W\,m^{-2}}$.

3.2. Optimization of channel networks for blockage tolerance

3.2.1. Optimization of the D4 design with a single blockage

Optimizations were first performed to minimize the panel temperature while the network was subject to a single worst-case blockage (the O_1 scheme). Fig. 7 presents optimization results for the 4-degree reference network ($D4\ R$) subject to a 2000 $\mathrm{W\,m^{-2}}$ applied heat flux and 28.2 $\mathrm{mL\,min^{-1}}$ flow rate. The clear reference network $R(\boldsymbol{c})$ has a T_{max} of 61.7 °C (Fig. 7a), which rises to 71.4 °C for the blocked case $R(\boldsymbol{w})$ (Fig. 7b). In contrast, the O_1 design has significantly lower T_{max} values of 48.4 °C when clear and 59.9 °C when blocked (Fig. 7c-d). The blocked O_1 design even outperforms the clear R design.

The pumping pressure and power predicted for the $R(\boldsymbol{c})$, $R(\boldsymbol{w})$, $O_1(\boldsymbol{c})$, and $O_1(\boldsymbol{w})$ panels using reduced channel dimensions are shown in Fig. S3. The pumping pressure and power are slightly lower for the optimized design (16 – 17 kPa) than the reference design (19 - 20 kPa). As expected, the pumping pressure and power increase slightly when a single blockage occurs.

To support the claim that Fig. 7d indeed displays the worst-case blockage in the set $\mathcal{B}$ for the O_1 design, Fig. S4 shows the temperature distributions for the blockages that give the six highest T_{max}

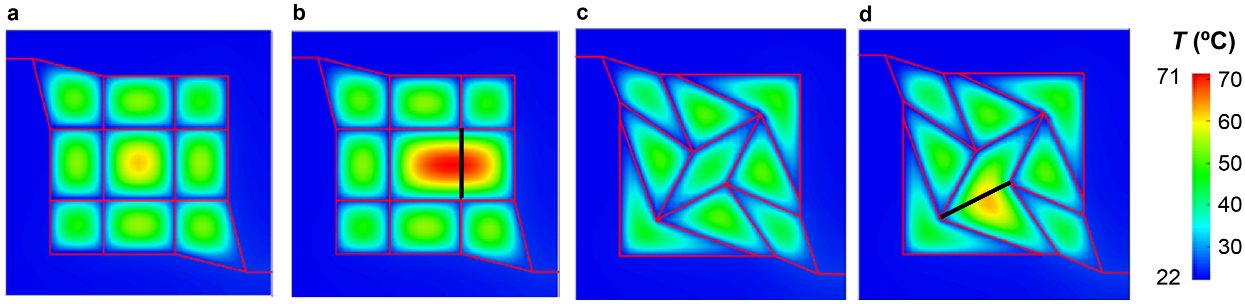

Figure 7: Improvement of blockage tolerance for the $D4$ R panel optimized with the O_1 technique. Simulated temperature profiles are shown for a) $R(\boldsymbol{c})$, b) $R(\boldsymbol{w})$, c) $O_1(\boldsymbol{c})$, and d) $O_1(\boldsymbol{w})$ panels at 2000 $\mathrm{W\,m^{-2}}$ applied heat flux and 28.2 $\mathrm{mL\,min^{-1}}$ flow rate. See Table 2 for panel notation. Blocked channels are colored in black.

values. The very similar T_{max} values of 59.92, 59.91, 59.78, 59.61, 59.54, and 59.45 °C demonstrate that the optimized design prevents any single blockage location from causing a particularly large temperature rise.

3.2.2. *Optimization across varying nodal degree*

Networks with interior nodal degrees of 2 - 6 were then optimized for both clear channels (O_0) and a single blockage (O_1). Fig. 8 compares the blockage-tolerance of designs optimized with the O_0 and O_1 schemes. The two schemes give similar temperature profiles for clear channels (the first and third columns). However, as apparent from the hot spots in the second and fourth columns, the O_1 designs perform substantially better than the O_0 designs when blocked.

The T_{max} values corresponding to the profiles in Fig. 8 are presented in Fig. 9. For clear channels, the $O_0(\boldsymbol{c})$ designs outperform the $O_1(\boldsymbol{c})$ designs, which is expected since O_0 designs were optimized for this case. The disparity in T_{max} is moderate for the $D2$ design (a 14 °C disparity) and otherwise relatively small (< 6 °C for all other nodal degrees). For both schemes, increasing nodal degree leads to decreasing T_{max} due to higher channel density.

For blocked channels, $O_1(\boldsymbol{w})$ designs outperform $O_0(\boldsymbol{w})$ designs for all nodal degree. The improvement in T_{max} is as high as 19 °C for the $D3$ design. Maximum temperature for $O_1(\boldsymbol{w})$ decreases steadily with increasing nodal degree due to both higher channel density and the presence of more paths to circumvent blockages. The most blockage-tolerant network, $D6$ O_1, has a T_{max} of 49 °C when blocked which is only 7 °C higher than when it is clear. In contrast, the least blockage-tolerant network $D2$ O_0 has a T_{max} of 90 °C when blocked which is 35 °C higher than when it is clear.

Fig. S5 presents values of cooling efficiency η for each panel in Fig. 8. Cooling efficiency ranges from 60% at low nodal degree to 85% at high nodal degree. As expected, O_1 panels maintain a higher value of η than O_0 panels when blocked.

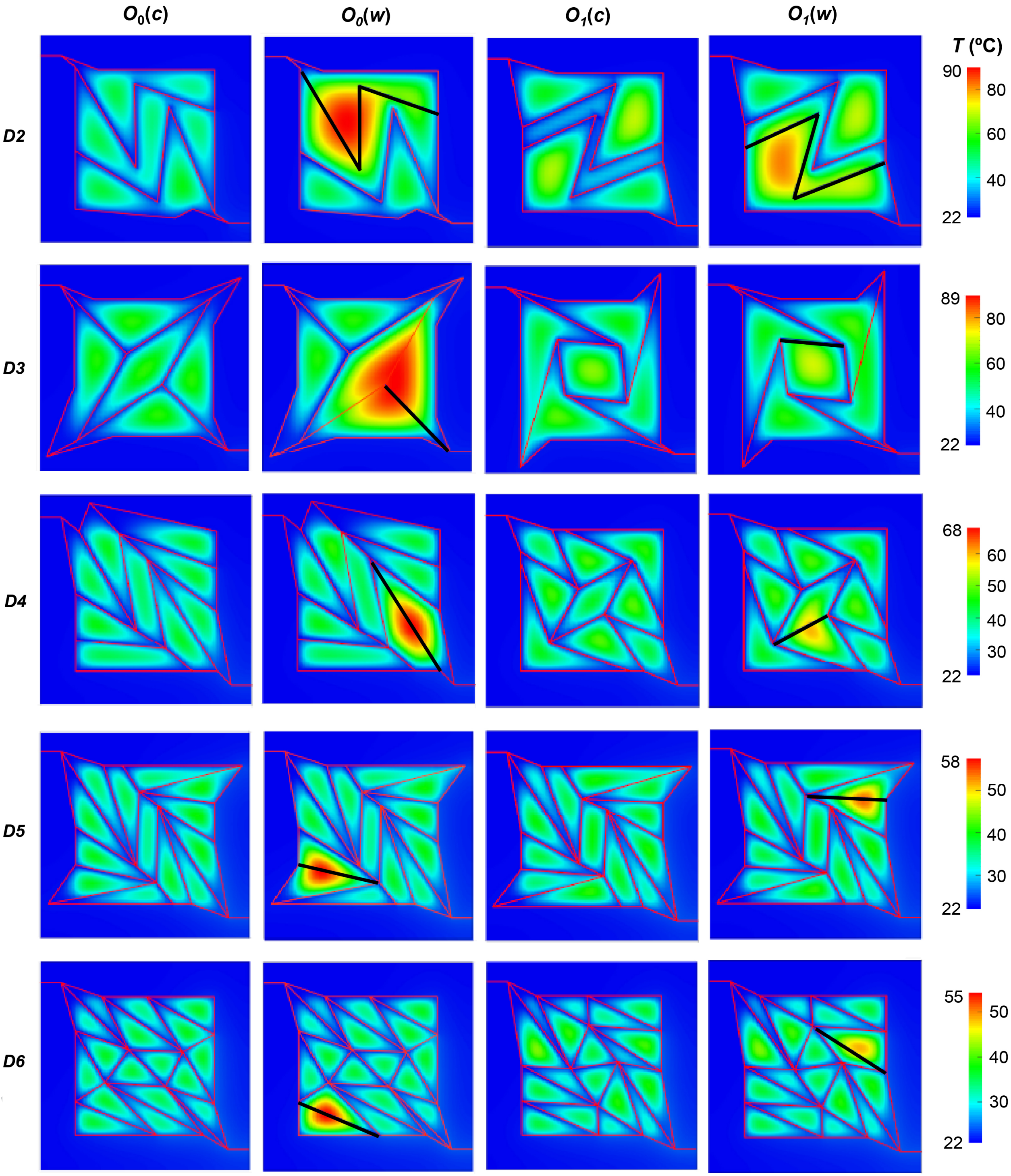

Figure 8: Comparison of panels optimized with the O_0 and O_1 techniques and nodal degrees of 2 – 6. Simulated thermal profiles are shown for both clear channels (first and third columns) and blocked channels (second and fourth columns) at 2000 $\mathrm{W\,m^{-2}}$ applied heat flux and 28.2 $\mathrm{mL\,min^{-1}}$ flow rate. Blocked channels are colored in black.

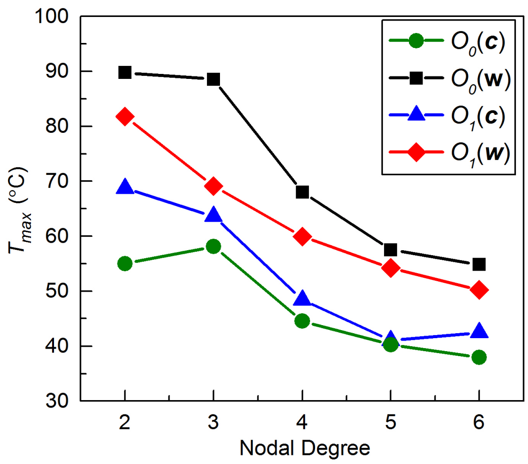

Figure 9: T_{max} as a function of nodal degree for the panels (O_0 and O_1) shown in Fig. 8 for both clear and single blockage scenarios. The applied heat flux is 2000 $\mathrm{W\,m^{-2}}$ and the flow rate is 28.2 $\mathrm{mL\,min^{-1}}$.

3.2.3. Optimization with different values of applied heat flux

The $D4$ panel was next optimized with the O_1 technique at a range of applied heat fluxes. Optimizations were performed for 1000 $\mathrm{W\,m^{-2}}$, 3000 $\mathrm{W\,m^{-2}}$, and 4000 $\mathrm{W\,m^{-2}}$ applied heat flux to compare to the baseline value of 2000 $\mathrm{W\,m^{-2}}$. The design optimized at 1000 $\mathrm{W\,m^{-2}}$ (Fig. S6a) was similar to the baseline design (Fig. S6b), and the designs optimized at 3000 $\mathrm{W\,m^{-2}}$ (Fig. S6c) and 4000 $\mathrm{W\,m^{-2}}$ (Fig. S6d) were nearly identical to the baseline design. The applied heat flux is seen to have a limited impact on the optimization process.

3.2.4. Optimization with a non-uniform heat flux

The $D4$ panel was then optimized with a non-uniform heat flux to demonstrate the versatility of the O_1 optimization technique. The localized heat source given by

$$f(x,y) = \begin{cases} q_o'' \left[1 - \left(\frac{x-x_o}{r_o}\right)^2\right]^2 \left[1 - \left(\frac{y-y_o}{r_o}\right)^2\right]^2 & |x - x_o| \leq r_o,\ |y - y_o| \leq r_o, \\ 0 & \text{otherwise}, \end{cases} \tag{6}$$

was applied over a 25 mm x 25 mm region in the top right of the panel (Fig. S7a). The geometric parameters were $r_o = 12.5$ mm and $x_o = y_o = 50$ mm. The total heating is $Q = \int_\Omega f(x,y)\mathrm{d}x\mathrm{d}y = (256 q_o'' r_o^2)/225$. The value of q_o'' was set to 28.125 $\mathrm{kWm^{-2}}$ so that $Q = 5$ W, the same total heating as the baseline case (a 50 mm x 50 mm heater producing 2 $\mathrm{kW}m^{-2}$). Fig. S7b-c shows the optimized design with clear and blocked channels. The optimization leads to channels being concentrated at the heated region as expected.

3.2.5. Optimization with two blockages

The $D6$ network was optimized while considering two blockages (the O_2 scheme) to demonstrate the generality of the optimization scheme. Fig. 10 compares thermal fields for the $D6$ O_0, O_1 and O_2 designs subject to a worst-case two-blockage scenario. For the O_0 and O_1 designs, a large hot spot develops in the right corner since the two blockages (shown in black) lead to a total of six channel segments with no flow (Fig. 10a-b). The O_2 design has increased channel density at the corners and the worst case dual blockage is now in the center region, leading to a much smaller T_{max} (Fig. 10c). A dual blockage in the right corner still leads to six channel segments with no flow (Fig. S8), but the resulting temperature increase is less than that from the center blockages.

Maximum temperature values for the three $D6$ designs under different blockage scenarios are compared in Fig. 10d. For the double blockage case, the $D6$ O_2 network has a 12 °C lower T_{max} compared to either O_0 and O_1 networks. As expected, each design has the lowest T_{max} in the scenario for which it was optimized.

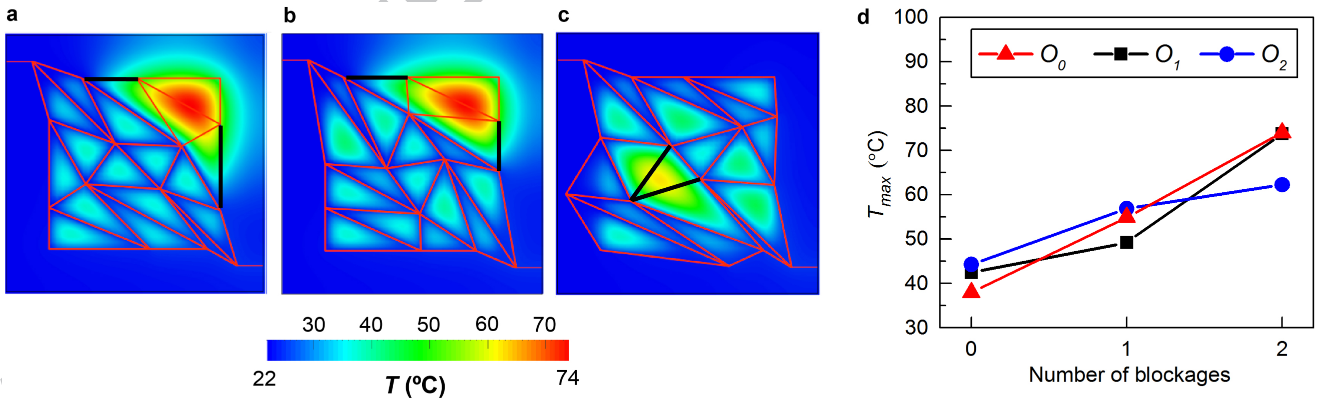

Figure 10: Response of $D6$ optimized designs to two simultaneous blockages. a) Thermal profiles for $O_0(\boldsymbol{w_2})$, b) $O_1(\boldsymbol{w_2})$, and c) $O_2(\boldsymbol{w_2})$ panels. The applied heat flux is 2000 $\mathrm{W\,m^{-2}}$ and the flow rate is 28.2 $\mathrm{mL\,min^{-1}}$. Blocked channels are colored in black. d) T_{max} for the same three designs with 0, 1, or 2 blockages.

3.3. Validation of optimized designs

Panels were fabricated with the $D2$, $D4$, and $D6$ O_1 designs to validate the blockage tolerance of these networks. Tests were performed on panels with both clear channels and the single worst-case blockage. Thermal profiles agree well between experiment and simulation for both clear channels (Fig. S9) and blocked channels (Fig. 11). Experiments reveal relatively uniform thermal profiles for clear channels (Fig. S9), the formation of hot spots due to blockages (Fig. 11), and decreasing panel temperature with increasing nodal degree for all cases.

Simulated and experimental T_{max} values are plotted vs. nodal degree in Fig. 12a. For the $D2$ design, T_{max} values agree within 5 °C. The disparity is attributed to uncertainty in the convection coefficient $\tilde{h}$, since a single value was chosen for all simulations, but $\tilde{h}$ likely increases with increasing panel temperature. For the $D4$ and $D6$ designs, T_{max} agrees within 2 °C which is within measurement error of the IR camera.

Pumping pressure and power are compared for the different networks in Fig. 12b. Pumping pressure and power decrease with increasing nodal degree due to shorter channel lengths and lower flow rates per channel. Experimental pressure values are bounded by simulations using average and reduced (one standard deviation) dimensions for the channel cross-section.

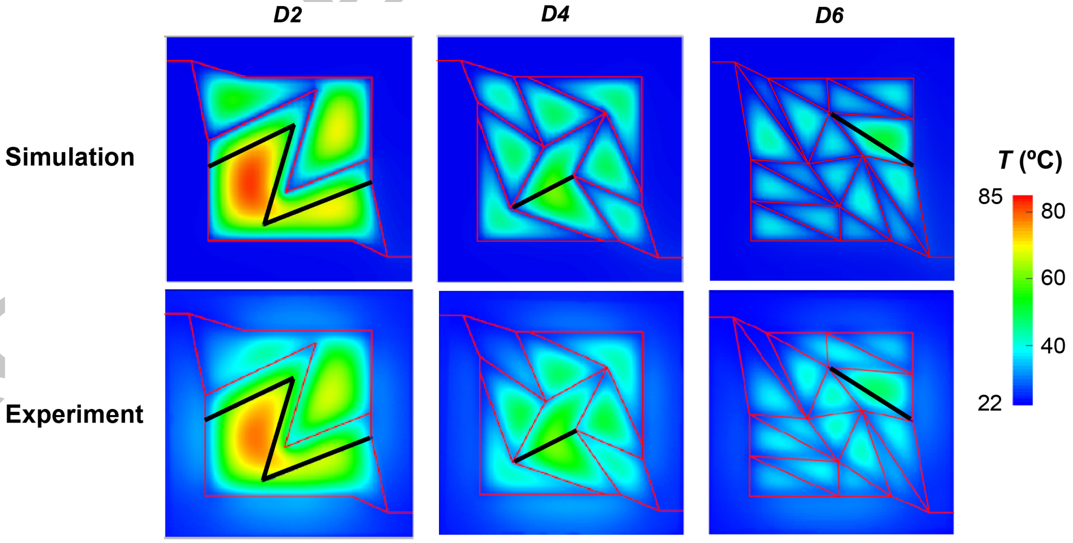

Figure 11: Comparison of simulated and experimental thermal profiles for $D2$, $D4$, and $D6$ $O_1(\boldsymbol{w})$ panels at 2000 W m^{-2} applied heat flux and 28.2 mL min^{-1} flow rate. Blocked channels are colored in black.

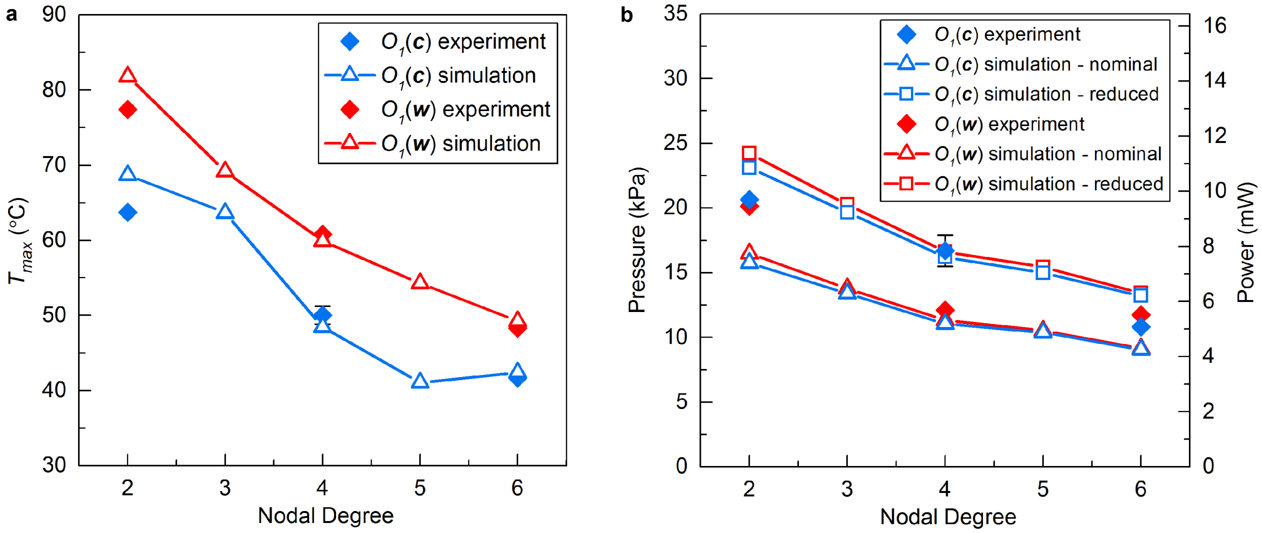

Figure 12: Validation of performance of $O_1(\boldsymbol{c})$ and $O_1(\boldsymbol{w})$ panels with different nodal degree. a) Experimental and simulated T_{max} values vs. nodal degree. b) Experimental pumping pressure compared to simulated values using both nominal channel dimensions (0.81 mm x 0.55 mm) and channel dimensions reduced by one standard deviation (0.68 mm x 0.53 mm). Experimental error bars represent the maximum and minimum values for three replicate panels for the $D4$ $O_1(\boldsymbol{c})$ case. The applied heat flux is 2000 $\mathrm{W\,m^{-2}}$ and the flow rate is 28.2 $\mathrm{mL\,min^{-1}}$.

4. Conclusions

This study was the first to optimize microvascular cooling networks for blockage tolerance. Microvascular PDMS cooling panels were simulated with high speed using dimensionally-reduced thermal and hydraulic models and the IGFEM technique. IR imaging of thermal experiments for a reference network design was used to validate the simulations over a range of flow rates. Vascular networks were then optimized by moving channel nodes to minimize the p-norm of temperature, a differentiable representation of T_{max}. Gradient-based optimizations were implemented while panels either had clear channels (O_0), the worst-case single blockage (O_1), or the worst-case dual blockages (O_2).

The O_0 and O_1 optimizations were performed on grid-based networks with interior nodal degrees (a measure of redundancy) from 2 – 6. The O_1 panels with high nodal degree displayed good tolerance of single blockages. For example, the $D6$ O_1 network exhibited a 7 °C rise in T_{max} when a single-channel was blocked at 2000 $\mathrm{W\,m^{-2}}$ applied heat flux, compared to a 35 °C rise for the $D2$ O_0 network. The magnitude of the applied heat flux was shown to have little influence on the

O_1 technique. However, the presence of a non-uniform heat flux leads to increased channel density near the heat source.

The O_2 scheme was performed for the $D6$ panel to design a network that could tolerate two blockages. The $D6$ O_2 network showed a 18 °C rise in T_{max} when subject to two blockages at 2000 $\mathrm{W\,m^{-2}}$ applied heat flux, compared to 36 °C and 31 °C rises for O_0 and O_1 networks, respectively. Thermal imaging provided experimental confirmation of blockage tolerance for O_1 designs. While this study considered vascular cooling panels, the optimization techniques presented here can be extended to design redundant microvascular networks for self-healing and other functions.

Acknowledgments

This work was supported by the National Science Foundation (CMMI 14-36720). The authors extend gratitude to Prof. Nancy Sottos for helpful discussion.

A. Appendix - Details for reduced-order solvers and IGFEM

A.1. Thermal and hydraulic reduced-order models

A.1.1. Reduced-order thermal model

The reduced-order thermal model was implemented as follows. Consider a channel with cross-sectional area A, axial velocity u and average velocity u_{ave}. Denoting the parametric coordinate along the channel in the flow direction s, the mass flow rate $\dot{m}$, and the specific heat capacity of the fluid c_p, the heat flow rate per unit length of the channel is given by [1, 37]

$$q' = \dot{m} c_p \frac{\mathrm{d}T_m}{\mathrm{d}s}, \tag{A1}$$

where T_m is the mixed-mean fluid temperature defined as $T_m = \int uT\mathrm{d}A/(Au_{\mathrm{ave}})$.

Now consider the domain denoted by Ω, which consists of a solid part Ω_s and a network of n_{ch} channels. Denote the curve representing channel i as $\Gamma_f^{(i)}$, the parametric representation of the curve as $\boldsymbol{x}^{(i)}(s)$, its unit tangent vector in the flow direction as $\boldsymbol{t}^{(i)}$, and the channel flow rate as $\dot{m}^{(i)}$. Given the thermal conductivity tensor $\boldsymbol{\kappa}$ of the solid Ω_s, a distributed heat source $f(\boldsymbol{x})$, the convection coefficient $\tilde{h}$, the emissivity ϵ and an ambient temperature T_∞, and denoting the Stefan-Boltzmann constant by σ_B, the following heat equation holds in Ω:

$$\nabla \cdot (\boldsymbol{\kappa} \nabla T) + f(\boldsymbol{x}) = \sum_{i=1}^{n_{ch}} \delta^{(i)}(\boldsymbol{x}) \gamma^{(i)} \boldsymbol{t}^{(i)} \cdot \nabla T + \tilde{h}(T - T_\infty) + \epsilon \sigma_B (T^4 - T_\infty^4), \tag{A2}$$

where $\gamma^{(i)} = \dot{m}^{(i)} c_p$ and $\delta^{(i)}(\boldsymbol{x}) = \int_{\Gamma_f^{(i)}} \delta(\boldsymbol{x} - \boldsymbol{x}^{(i)}(s)) \mathrm{d}s$ is the line Dirac delta function associated with channel i. Details of the assumptions underlying this equation can be found in [1, 38].

The boundary of Ω is partitioned into Γ_T and Γ_q, where Dirichlet and Neumann boundary conditions are respectively specified, and the prescribed heat flux on Γ_q is $q''^{(p)}$. The weak form of (A2) is as follows: find the temperature field T satisfying the Dirichlet boundary condition $T_{|\Gamma_T} = T^{(p)}$ such that $\forall v \in \mathbb{V}$,

$$\begin{aligned} 0 = &- \int_{\Omega_s} \nabla v \cdot \boldsymbol{\kappa} \nabla T \mathrm{d}\Omega - \int_{\Omega_s} v(\tilde{h}T + \epsilon \sigma_B T^4) \mathrm{d}\Omega - \sum_{i=1}^{n_{ch}} \int_{\Gamma_f^{(i)}} v \gamma^{(i)} \boldsymbol{t}^{(i)} \cdot \nabla T \mathrm{d}\Gamma \\ &+ \int_{\Omega_s} v f \mathrm{d}\Omega + + \int_{\Omega_s} v(\tilde{h} T_\infty + \epsilon \sigma_B T_\infty^4) \mathrm{d}\Omega + \int_{\Gamma_q} v q''^{(p)} \mathrm{d}\Gamma, \end{aligned} \tag{A3}$$

where $\mathbb{V}$ is the space of weight functions. The Streamline Upwind/Petrov-Galerkin (SUPG) scheme is applied to stabilize the solution [1].

A.1.2. Reduced-order hydraulic model

Fluid pressure and flow division were calculated as follows. For a network of channels, the mass flow rate in each channel was obtained by first solving for the pressure P_j at each end point or node of the channel network using a system of hydraulics equations, which were assembled from the following relation between the nodal pressures, P_j, P_k of channel i and the contribution of its flow rate $S_j^{(i)}, S_k^{(i)}$ to the nodes j, k [39]:

$$g^{(i)} \begin{bmatrix} 1 & -1 \\ -1 & 1 \end{bmatrix} \begin{Bmatrix} P_j \\ P_k \end{Bmatrix} = \begin{Bmatrix} S_j^{(i)} \\ S_k^{(i)} \end{Bmatrix}, \tag{A4}$$

where $g^{(i)}$ is the conductance of channel i. For a rectangular cross section with height a, width b ($b \geq a$) and length L_{ch} containing a fluid with kinematic viscosity ν, the conductance is given by

[33]

$$g^{(i)} = \frac{a^3 b}{4\nu L_{ch}}\left[\frac{1}{3} - \frac{64a}{\pi^5 b}\tanh\left(\frac{\pi b}{2a}\right)\right], \tag{A5}$$

where ν is a function of the average temperature of the coolant. If P_j and P_k are the pressures at the two nodes j and k of channel i, the mass flow rate in channel i is given by $\dot{m}^{(i)} = g^{(i)}|P_j - P_k|$.

A.2. Interface-enriched generalized finite element method (IGFEM)

Simulations were performed using an interface-enriched generalized finite element method (IGFEM) solver. The weak form of (A3) was discretized by approximating $\mathbb{V}$ with a finite-dimensional space, defined by the mesh and the shape functions. For the standard finite element method, a mesh that conforms to the channels is needed to capture the discontinuous temperature gradients across the microchannels. However, generating a conforming mesh for dense, branching channel networks is complex and costly. Furthermore, as the microchannel configuration evolves during shape optimization, a method that requires a conforming mesh is prone to severe mesh distortion and thus requires frequent remeshing. Hence IGFEM was adopted to capture the discontinuous gradients of the thermal field with non-conforming meshes [40, 41]. Let the number of original nodes of the non-conforming mesh be n_{on}, with T_i and $N_i(\boldsymbol{x})$ respectively denoting the nodal temperature value and the Lagrangian shape function associated with node i. In the IGFEM formulation, enrichment nodes with associated enrichment functions ψ_j and generalized degrees of freedom β_j (with $j = 1, 2, ..., n_{en}$) were introduced along the channels, yielding the following approximation for the temperature field:

$$T^{(h)}(\boldsymbol{x}) = \sum_{i=1}^{n_{on}} T_i N_i(\boldsymbol{x}) + \sum_{j=1}^{n_{en}} \beta_j \psi_j(\boldsymbol{x}) = \begin{Bmatrix} \{N(\boldsymbol{x})\} \\ \{\psi(\boldsymbol{x})\} \end{Bmatrix}' \begin{Bmatrix} \{T\} \\ \{\beta\} \end{Bmatrix}, \tag{A6}$$

where $\{\cdot\}'$ denotes the transpose of the vector $\{\cdot\}$.

For conciseness, we hereafter omit the distinction between original and enrichment degrees of freedom as well as between original shape functions and enrichment functions, and rewrite (A6) as

$$T^{(h)}(\boldsymbol{x}) = \{N(\boldsymbol{x})\}'\{T\}. \tag{A7}$$

Let $[B]$ be the matrix of the spatial derivative of $\{N\}$ with each column corresponding to the derivative with respect to a coordinate. Furthermore, let the vector of weight function be $\{W\}$, 420 whose expression can be found in [1]. Note that $\{W\}$ is different from the shape functions $\{N\}$ in this work since SUPG is used. Substituting the approximate temperature field (A6) and weight function into the weak form (A3), the discretized weak form is given by

$$[K(\{T\})]\{T\} = \{F\}, \tag{A8}$$

where

$$\begin{aligned}[K(\{T\})] = &\int_{\Omega_s} [B][\kappa][B]'\mathrm{d}\Omega + \int_{\Omega_s} (\tilde{h} + \epsilon\sigma_B T^{(h)3})\{W\}\{N\}'\mathrm{d}\Omega \\ &+ \sum_{i=1}^{n_{ch}} \int_{\Gamma_f^{(i)}} \{W\}([B]\gamma^{(i)}\{t^{(i)}\})'\mathrm{d}\Gamma,\end{aligned} \tag{A9}$$

and

$$\{F\} = \int_{\Omega_s} \{W\} f \mathrm{d}\Omega + \int_{\Omega_s} \{W\}(\tilde{h}T_\infty + \epsilon\sigma_B T_\infty^4)\mathrm{d}\Omega + \int_{\Gamma_q} \{N\} q''^{(p)}\mathrm{d}\Gamma. \tag{A10}$$

The expressions of the stiffness matrix $[K(\{T\})]$ and load vector $\{F\}$ for IGFEM can be found 425 in [42]. The radiation terms were linearized during optimizations for efficiency, i.e., $q''_{rad} = \epsilon\sigma_B(T^4 - T_\infty^4)$ was replaced with $q''_{rad} = 4\epsilon\sigma_B T_\infty^3(T - T_\infty)$. This allowed the nonlinear terms in the foregoing equations (A2), (A3), (A9) and (A10) to be removed and $\tilde{h}$ to be substituted with $\tilde{h} + 4\epsilon\sigma_B T_\infty^3$, leading to a linear system of equations.

After optimizations were complete, the nonlinear thermal model was solved for the final designs 430 to give greater accuracy. The solution to the nonlinear model was obtained using the procedure outlined in Algorithm 1. Unlike nonlinear structural mechanics, no incremental loading is required.

The Newton-Raphson method obtains the solution at iteration $n+1$ by linearizing the system of equations about the solution at iteration n to yield the following equation:

$$[J(\{T^{(n)}\})](\{T^{(n+1)}\} - \{T^{(n)}\}) = \{R(\{T^{(n)}\})\}, \tag{A11}$$

Algorithm 1 Iterative procedure for solving nonlinear equation.

```
Set termination tolerance $\varepsilon$
Initialize $\{T^{(0)}\}$
$n = 0, d_0 = 1, l_0 = 0$
while $d_n > \varepsilon l_n$ do
    Use Newton-Raphson method to obtain $\{T^{(n+1)}\}$
    $l_n = \|\{T^{(n+1)}\}\|_2$
    $d_n = \|\{T^{(n+1)}\} - \{T^{(n)}\}\|_2$
    $n = n + 1$
end while
```

where

$$J_{ik}(\{T^{(n)}\}) = K_{ik}(\{T^{(n)}\}) + \frac{\partial K_{ij}}{\partial T_k^{(n)}} T_j^{(n)}, \tag{A12}$$

and

$$\{R(\{T^{(n)}\})\} = \{F\} - [K(\{T^{(n)}\})]\{T^{(n)}\}. \tag{A13}$$

References

[1] M. H. Tan, A. R. Najafi, S. J. Pety, S. R. White, P. H. Geubelle, Gradient-based design of actively-cooled microvascular composite panels, Int. J. Heat Mass Transf. 103 (2016) 594–606.

[2] S. J. Pety, P. X. L. Chia, S. M. Carrington, S. R. White, Active cooling of microvascular composites for battery packaging, Smart. Mater. Struct. 26 (2017) 105004.

[3] S. J. Pety, M. H. Tan, A. R. Najafi, P. R. Barnett, N. R. Sottos, P. H. Geubelle, S. R. White, Carbon fiber composites with 2D microvascular networks for battery cooling, Int. J. Heat Mass Transf. 115 (2017) 513–522.

[4] A. Jarrett, I. Y. Kim, Design optimization of electric vehicle battery cooling plates for thermal performance, J. Power Sources 196 (23) (2011) 10359–10368.

[5] S. H. Yu, S. Sohn, J. H. Nam, C.-J. Kim, Numerical study to examine the performance of multi-pass serpentine flow-fields for cooling plates in polymer electrolyte membrane fuel cells, J. Power Sources 194 (2) (2009) 697–703.

[6] G. Zhang, S. G. Kandlikar, A critical review of cooling techniques in proton exchange membrane fuel cell stacks, Int. J. Hydrogen Energy 37 (3) (2012) 2412–2429.

[7] B. Ramos-Alvarado, P. Li, H. Liu, A. Hernandez-Guerrero, CFD study of liquid-cooled heat sinks with microchannel flow field configurations for electronics, fuel cells, and concentrated solar cells, Appl. Therm. Eng. 31 (14-15) (2011) 2494–2507.

[8] A. M. Coppola, A. S. Griffin, N. R. Sottos, S. R. White, Retention of mechanical performance of polymer matrix composites above the glass transition temperature by vascular cooling, Compos. Part A Appl. Sci. Manuf. 78 (2015) 412–423.

[9] A. Coppola, L. Hu, P. Thakre, M. Radovic, I. Karaman, N. Sottos, S. White, Active Cooling of a Microvascular Shape Memory Alloy-Polymer Matrix Composite Hybrid Material, Adv. Eng. Mater. 18 (7) (2016) 1145–1153.

[10] A. M. Coppola, L. G. Warpinski, S. P. Murray, N. R. Sottos, S. R. White, Survival of actively cooled microvascular polymer matrix composites under sustained thermomechanical loading, Compos. Part A Appl. Sci. Manuf. 82 (2016) 170–179.

[11] S. Soghrati, A. R. Najafi, J. H. Lin, K. M. Hughes, S. R. White, N. R. Sottos, P. H. Geubelle, Computational analysis of actively-cooled 3D woven microvascular composites using a stabilized interface-enriched generalized finite element method, Int. J. Heat Mass Transf. 65 (2013) 153–164.

[12] C. Hansen, Microvascular-based self-healing materials, in: G. Li, H. Meng (Eds.), Recent Adv. Smart Self-healing Polym. Compos., Elsevier Ltd., Cambridge, 2015, pp. 129–157.

[13] N. Sakurayama, S. Minakuchi, N. Takeda, Sensing and healing of disbond in composite stiffened panel using hierarchical system, Compos. Struct. 132 (2015) 833–841.

[14] A. P. Esser-Kahn, P. R. Thakre, H. Dong, J. F. Patrick, V. K. Vlasko-Vlasov, N. R. Sottos, J. S. Moore, S. R. White, Three-dimensional microvascular fiber-reinforced composites, Adv. Mater. 23 (32) (2011) 3654–8.

[15] D. J. Hartl, G. J. Frank, G. H. Huff, J. W. Baur, A liquid metal-based structurally embedded vascular antenna : I . Concept and multiphysical modeling, Smart Mater. Struct. 26 (2016) 025002.

[16] S. G. Kandlikar, High Flux Heat Removal with Microchannels: A Roadmap of challenges and opportunities, Heat Transf. Eng. 26 (8) (2005) 5–14.

[17] R. S. Bunker, Gas turbine cooling: moving from macro to micro cooling, in: ASME Turbomachinery Expo, 2013, pp. 1–17.

[18] H. G. Kerkhoff, H. P. A. Hendriks, Fault Modeling and Fault Simulation in Mixed Micro-Fluidic Microelectronic Systems, J. Electron. Test. Theory Appl. 17 (2001) 427–437.

[19] C. Amador, A. Gavriilidis, P. Angeli, Flow distribution in different microreactor scale-out geometries and the effect of manufacturing tolerances and channel blockage, Chem. Eng. J. 101 (2004) 379–390.

[20] X.-Q. Wang, A. S. Mujumdar, C. Yap, Numerical Analysis of Blockage and Optimization of Heat Transfer Performance of Fractal-like Microchannel Nets, J. Electron. Packag. 128 (1) (2006) 38.

[21] H. R. Williams, R. S. Trask, A. C. Knights, E. R. Williams, I. P. Bond, Biomimetic reliability strategies for self-healing vascular networks in engineering materials., J. R. Soc. Interface 5 (24) (2008) 735–47.

[22] L. Sack, E. M. Dietrich, C. M. Streeter, D. Sánchez-Gómez, N. M. Holbrook, Leaf palmate venation and vascular redundancy confer tolerance of hydraulic disruption., PNAS 105 (5) (2008) 1567–1572.

[23] C. B. Schaffer, B. Friedman, N. Nishimura, L. F. Schroeder, P. S. Tsai, F. F. Ebner, P. D. Lyden, D. Kleinfeld, Two-photon imaging of cortical surface microvessels reveals a robust redistribution in blood flow after vascular occlusion, PLoS Biol. 4 (2) (2006) 258–270.

[24] P. Blinder, A. Y. Shih, C. Rafie, D. Kleinfeld, Topological basis for the robust distribution of blood to rodent neocortex, PNAS 107 (28) (2010) 12670–12675.

[25] P. Blinder, P. S. Tsai, J. P. Kaufhold, P. M. Knutsen, H. Suhl, D. Kleinfeld, The cortical angiome : an interconnected vascular network with noncolumnar patterns of blood flow, Nat. Neurosci. 16 (7) (2013) 889–897.

[26] E. Katifori, G. J. Szöllosi, M. O. Magnasco, Damage and fluctuations induce loops in optimal transport networks, Phys. Rev. Lett. 104 (4) (2010) 048704.

[27] F. Corson, Fluctuations and Redundancy in Optimal Transport Networks, Phys. Rev. Lett. 104 (4) (2010) 048703.

[28] A. M. Aragón, J. K. Wayer, P. H. Geubelle, D. E. Goldberg, S. R. White, Design of microvascular flow networks using multi-objective genetic algorithms, Comput. Methods Appl. Mech. Eng. 197 (2008) 4399–4410.

[29] S. Senn, D. Poulikakos, Laminar mixing, heat transfer and pressure drop in tree-like microchannel nets and their application for thermal management in polymer electrolyte fuel cells, J. Power Sources 130 (2004) 178–191.

[30] M. H. Tan, M. Safdari, A. R. Najafi, P. H. Geubelle, A NURBS-based interface-enriched generalized finite element scheme for the thermal analysis and design of microvascular composites, Comput. Methods Appl. Mech. Eng. 283 (2015) 1382–1400.

[31] J. G. Michopoulos, B. Dennis, A. I. Foteini Komninelli, A. Akbariyeh, Performance of reduced order models of moving heat source deposition problems for efficient inverse analysis, in: ASME 2014 Int. Des. Eng. Tech. Conf. & Comput. Inf. Eng. Conf., 2014, pp. DETC/CIE2014–35365.

[32] Dow Corning Sylgard ® 184 Silicone Elastomer data sheet.

[33] M. Bahrami, M. M. Yovanovich, J. R. Culham, Pressure Drop of Fully- Developed Laminar Flow in Microchannels of Arbitrary Cross-Section, J. Fluids Eng. 128 (2006) 1036–1044.

[34] P. T. Boggs, J. W. Tolle, Sequential Quadratic Programming, Acta Numer. 4 (1995) 1–52.

[35] A. D. Waren, L. S. Lasdon, D. F. Suchman, Optimization in Engineering Design, Proc. IEEE 55 (11) (1967) 1885–1897.

[36] C. Charalambous, A. R. Conn, An efficient method to solve the minimax problem directly, SIAM J. Numer. Anal. 15 (1) (1978) 162–187.

[37] W. M. Kays, M. E. Crawford, Convective Heat and Mass Transfer, McGraw-Hill, New York, 1993.

[38] M. H. Tan, P. H. Geubelle, 3d reduced-order modeling and gradient-based optimization of embedded microchannels for active cooling, Comput. Methods Appl. Mech. Eng. (2017) in review.

[39] C. A. Brebbia, A. J. Ferrante, Computational Hydraulics, Butterworths, London, 1983.

[40] S. Soghrati, A. M. Aragón, C. A. Duarte, P. H. Geubelle, An interface-enriched generalized FEM for problems with discontinuous gradient fields, Int. J. Numer. Methods Eng. 89 (2012) 991–1008.

[41] S. Soghrati, P. H. Geubelle, A 3D interface-enriched generalized finite element method for weakly discontinuous problems with complex internal geometries, Comput. Methods Appl. Mech. Eng. 217-220 (2012) 46–57.

[42] A. R. Najafi, M. Safdari, D. A. Tortorelli, P. H. Geubelle, A gradient-based shape optimization scheme using an interface-enriched generalized FEM, Comput. Methods Appl. Mech. Eng. 296 (2015) 1–17.